Four-Sublattice Chiral Ordering and Emergent Multipole Degrees of Freedom on a Triangular Lattice

Satoru Hayami *

Posted Date: 10 November 2025

doi: 10.20944/preprints202511.0660.v1

Keywords: chiral spin ordering; Berry curvature; multipole moment; multiple-Q states; density waves; triangular lattice

 doi:10.20944/preprints202511.0660.v1

Article

Four-Sublattice Chiral Ordering and Emergent Multipole Degrees of Freedom on a Triangular Lattice

Satoru Hayami [1]

Graduate School of Science, Hokkaido University, Sapporo 060-0810, Japan; hayami@phys.sci.hokudai.ac.jp

Abstract

Chiral magnetic orderings in itinerant magnets have recently attracted considerable attention as a source of emergent electromagnetic phenomena such as topological Hall effects and magnetoelectric couplings. In this study, we investigate emergent multipole degrees of freedom arising from chiral magnetic orderings on a two-dimensional triangular lattice. Focusing on a four-sublattice spin configuration characterized by noncoplanar spin textures, we demonstrate that various types of multipoles, such as magnetic dipoles and electric toroidal dipoles, naturally emerge even in the absence of relativistic spin–orbit coupling. By employing a microscopic tight-binding model, we classify the resulting multipole moments and clarify their relationships to the underlying chiral spin texture. We further explore how spin–orbit coupling modifies these multipole characters, leading to additional uniform responses. The results provide a unified framework connecting noncollinear magnetic orderings and emergent multipole phenomena, offering insights into unconventional cross-correlation phenomena in itinerant chiral magnets.

Keywords: chiral spin ordering; Berry curvature; multipole moment; multiple-Q states; density waves; triangular lattice

1. Introduction

Chiral magnetic orderings have become a central topic in modern condensed matter physics owing to their capability to host emergent electromagnetic phenomena [1–7] and nonlinear nonreciprocal transport [8–12]. In particular, the interplay between geometrical frustration and itinerant magnetism on two/three-dimensional lattices has revealed a rich variety of noncoplanar spin textures with scalar spin chirality [13–16]. Among them, four-sublattice chiral orderings, in which spins form a noncoplanar arrangement within the 2×2 magnetic unit cell, have been widely studied as prototypical examples of spin configurations giving rise to finite Berry curvature and nontrivial topological transport [17–20]. These chiral states are generally characterized as multiple-Q magnetic orderings, where several spin modulation vectors coherently superpose to produce a periodic noncoplanar spin texture [21–24]. Such states with short-range magnetic periods can appear in triangular [17,18,25–28], kagome [29,30], and face-centered-cubic lattices [31,32], stabilized by competing exchange interactions, multi-spin interactions, and Fermi surface nesting [33–35].

Previous studies have shown that such four-sublattice spin textures can carry a finite Chern number in the electronic band structure, leading to the topological Hall effect in the absence of spin–orbit coupling [17,18]. This emergent Hall response originates from the real-space Berry curvature associated with the scalar spin chirality, which acts as an effective magnetic field for itinerant electrons [36–40]. Consequently, the four-sublattice chiral order provides a minimal platform to study topological transport without relying on relativistic effects. Moreover, this type of spin arrangement is closely related to magnetic skyrmions [41–43], since both share the same topological invariant and can be viewed as periodic arrays of local noncoplanar spin configurations. Experimental realizations of skyrmion crystals in a variety of materials under distinct lattice structures have further motivated theoretical investigations of such multiple-Q chiral states on frustrated lattices. Indeed, the skyrmion crystals

 doi:10.20944/preprints202511.0660.v1

have been identified not only in noncentrosymmetric magnetic compounds like MnSi [44–51], other B20-type compounds [52–65], and polar compounds [66–70] but also in centrosymmetric compounds like Gd_2PdSi_3 [71–76] and $Gd_3Ru_4Al_{12}$ [77–80].

Beyond their topological transport properties, chiral magnetic structures are also of great interest from the viewpoint of emergent multipole degrees of freedom [81–85]. In systems with complicated spin orderings, the spatial distribution of spin and orbital moments can be expressed in terms of multipoles that capture the symmetry and cross-correlation responses of the state [86]. Recent theoretical works have extended the concept of multipoles to include magnetic toroidal and electric toroidal multipoles [85], which account for various unconventional physical quantities like ferroaxial moments [87]. Such a multipole description provides a unified way to understand a variety of cross-correlation effects, including the anomalous Hall effect, the magnetoelectric effect, and the nonreciprocal transport phenomena.

In itinerant magnets, the emergence of multipoles is intimately related to momentum-dependent spin textures. In particular, noncollinear and noncoplanar spin configurations give rise to distinct multipole degrees of freedom that serve as microscopic sources of various cross-correlation physical phenomena. For instance, noncollinear spin textures characterized by vector spin chirality can induce electric dipole moments, leading to antisymmetric spin splitting in the electronic band structure [88–90], resulting electric polarization [91–95] and spin Hall effect [96–100]. Meanwhile, noncoplanar spin textures characterized by scalar spin chirality generate magnetic dipoles responsible for the anomalous Hall effect [1,31], as well as magnetic toroidal dipoles responsible for nonreciprocal transport [8–12]. The four-sublattice chiral state on a triangular lattice provides an ideal platform to elucidate how such multipole moments emerge and interplay, since its inherently noncoplanar spin configuration breaks time-reversal symmetry even in the absence of relativistic spin–orbit coupling.

In this study, we theoretically investigate the emergent multipole degrees of freedom associated with a four-sublattice chiral magnetic structure on a two-dimensional triangular lattice. Using a microscopic tight-binding model, we analyze the resulting orbital and spin-dependent multipole moments, such as magnetic dipoles, anisotropic magnetic dipoles, electric monopoles, and electric toroidal dipoles. We show that the noncoplanar spin arrangement induces these multipoles even in the absence of spin–orbit coupling, reflecting the complicated spin texture. Furthermore, when spin–orbit coupling is introduced, uniform components of multipole moments additionally appear, leading to new cross-correlation responses that bridge chiral magnetism and multipole physics. Our findings provide a relationship among chiral spin order, cross-correlation effect, and multipole physics, offering fundamental insight into emergent physical phenomena in frustrated itinerant magnets.

The rest of this paper is organized as follows. Section 2 formulates the s–p orbital tight-binding model on a two-dimensional triangular lattice. We also introduce triple-Q chiral spin textures corresponding to the four-sublattice noncoplanar magnetic ordering. Section **??** presents the results obtained without relativistic spin–orbit coupling, where the emergence of orbital magnetic dipoles, spin and anisotropic magnetic dipoles, spin-dependent electric monopoles, and electric toroidal dipoles are analyzed in both real and momentum spaces. The effective spin–orbit interaction and the resulting ferroaxial moment are also discussed. Section **??** examines the effects of introducing spin–orbit coupling on these multipoles and demonstrates how new uniform components arise, modifying the symmetry and intensity distributions of the multipole structure factors. Finally, Sec. 5 summarizes the key findings and provides perspectives on possible extensions of this work to other frustrated magnetic systems.

2. Setup

We study a minimal tight-binding model that captures the essential features of four-sublattice chiral magnetic order and its associated multipole degrees of freedom on a two-dimensional triangular lattice. The system possesses spatial inversion symmetry and belongs to the point group D_{6h}. We set the lattice constant to unity. To investigate the relationship between chiral spin ordering and

 doi:10.20944/preprints202511.0660.v1

multipoles, we consider multi-orbital degrees of freedom consisting of s and p orbitals, since the Hilbert space spanned by these orbitals includes a variety of multipole degrees of freedom [101]. The model Hamiltonian is written as

$$\mathcal{H} = -\sum_{ij\alpha\alpha'\sigma}\left(t_{ij}^{\alpha\alpha'}c_{i\alpha'\sigma}^{\dagger}c_{j\alpha\sigma} + \text{H.c.}\right) + \lambda\sum_{i\tilde{\alpha}\tilde{\alpha}'\sigma\sigma'}c_{i\tilde{\alpha}\sigma}^{\dagger}H_{\tilde{\alpha}\tilde{\alpha}'}^{\text{SOC}}c_{i\tilde{\alpha}'\sigma'} + J\sum_{i\alpha\sigma\sigma'}c_{i\alpha\sigma}^{\dagger}\boldsymbol{\sigma}_{\sigma\sigma'}c_{i\alpha\sigma'}\cdot\boldsymbol{S}_i. \tag{1}$$

Here, $c_{i\alpha\sigma}^{\dagger}$ ($c_{i\alpha\sigma}$) creates (annihilates) an electron at lattice site i with spin σ in orbital $\alpha = s, p_x, p_y, p_z$ (or $\tilde{\alpha} = p_x, p_y, p_z$). The first term describes the electron hopping between neighboring orbitals. To respect the $D_{6\text{h}}$ symmetry of the triangular lattice, we include the nearest-neighbor hopping amplitudes t_s for s–s orbitals, $t_{p\sigma}$ and $t_{p\pi}$ for (p_x, p_y, p_z) orbitals, and t_{sp} for s–p orbital hybridization following the Slater-Koster parameters. Orbital-dependent onsite potentials are neglected for simplicity.

The second term in Eq. (1) represents the atomic spin–orbit coupling acting on the p orbitals. Its matrix form is given by

$$H^{\text{SOC}} = \frac{1}{2}\begin{pmatrix} 0 & -i\sigma^z & i\sigma^y \\ i\sigma^z & 0 & -i\sigma^x \\ -i\sigma^y & i\sigma^x & 0 \end{pmatrix}, \tag{2}$$

where σ^{μ} ($\mu = x, y, z$) are the Pauli matrices. Throughout this work, we set $t_s = -1$ as the energy unit and use $t_{p\sigma} = 0.7$, $t_{p\pi} = 0.4$, $t_{sp} = 0.6$, and $\lambda = 0$ or 0.5 to compare the cases without and with spin–orbit coupling.

The last term in Eq. (1) describes the exchange interaction between itinerant electrons and localized magnetic moments $\boldsymbol{S}_i$, with the coupling strength J. We assume that $\boldsymbol{S}_i$ forms a four-sublattice noncoplanar chiral structure on the triangular lattice, as schematically illustrated in Figure 1. This configuration can be represented as a coherent superposition of three symmetry-related spin density waves with modulation vectors $\boldsymbol{Q}_1 = (0, Q)$, $\boldsymbol{Q}_2 = (-\sqrt{3}Q/2, -Q/2)$, and $\boldsymbol{Q}_3 = (\sqrt{3}Q/2, -Q/2)$ with $Q = 2\pi/\sqrt{3}$ that are located at the M point in the Brillouin zone. In other words, this state corresponds to a triple-Q magnetic state. In real space, the spins on the four sublattices are oriented so as to form a regular tetrahedron, as shown in the right panel of Figure 1. We specifically set $\boldsymbol{S}_{\text{A}} = (0, 0, 1)$, $\boldsymbol{S}_{\text{B}} = (0, -2\sqrt{2}/3, -1/3)$, $\boldsymbol{S}_{\text{C}} = (-\sqrt{2/3}, \sqrt{2}/3, -1/3)$, and $\boldsymbol{S}_{\text{D}} = (\sqrt{2/3}, \sqrt{2}/3, -1/3)$. The spin texture thereby acquires a finite scalar spin chirality, $\boldsymbol{S}_i \cdot (\boldsymbol{S}_j \times \boldsymbol{S}_k)$, which acts as an emergent magnetic flux on itinerant electrons. Consequently, the electronic bands carry a quantized Chern number, giving rise to a finite Berry curvature and a topological Hall effect even in the absence of relativistic spin–orbit coupling.

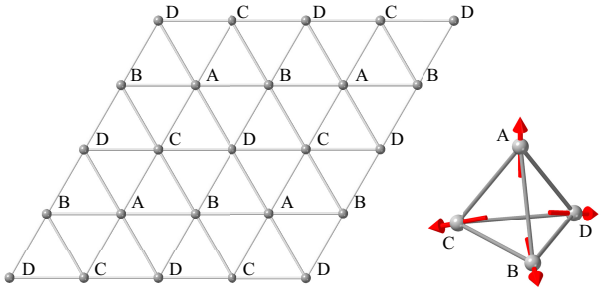

Figure 1. Four-sublattice magnetic structure on a two-dimensional triangular lattice. The direction of spin moments at each sublattice is shown in the right panel, where the red arrows represent the spin moment.

Such four-sublattice chiral orderings constitute one of the simplest microscopic realizations of chiral topological magnets with a quantized Chern number. They are energetically stabilized by various microscopic mechanisms, such as ring exchange interactions [33] and positive biquadratic interactions [34], the latter of which originates from the nesting of the Fermi surfaces in itinerant electron systems and plays an important role in inducing multiple-Q instabilities, including vortex

 doi:10.20944/preprints202511.0660.v1

crystals, as found in $Y_3Co_8Sn_4$ [102]. Experimentally, similar chiral states have been identified in several materials, such as Co_xTaS_2 [103–105].

3. Results Without the Spin–Orbit Coupling

In this section, we focus on the case without relativistic spin–orbit coupling ($\lambda = 0$) in order to clarify how the four-sublattice chiral spin texture itself generates various multipole degrees of freedom. The calculations are performed for the chemical potential $\mu = -2$ and exchange coupling $J = 1$, unless stated otherwise. Even in the absence of spin–orbit coupling, the noncoplanar spin texture acts as an effective magnetic field through the scalar spin chirality, thereby inducing nontrivial spin–orbital hybridization and emergent multipole moments. We examine in detail the orbital magnetic, spin magnetic, anisotropic magnetic, spin-dependent electric, and electric toroidal multipoles arising from the chiral spin background.

3.1. Orbital Magnetic Dipole

Figure 2(a) shows the structure factor of the orbital magnetic dipole $\boldsymbol{M}$, which is obtained by diagonalizing the Hamiltonian for the $N = 2 \times 2$ sites and the 1200×1200 supercells under the periodic boundary conditions. Here, the structure factor in terms of the orbital magnetic dipole for the μ component is defined as

$$\tilde{M}_\mu(\boldsymbol{q}) = \frac{1}{N}\sum_{ij}\langle M_\mu\rangle_i\langle M_\mu\rangle_j e^{i\boldsymbol{q}\cdot(\boldsymbol{r}_i-\boldsymbol{r}_j)}, \tag{3}$$

where $\boldsymbol{q}$ is the wave vector in the Brillouin zone, $\boldsymbol{r}_i$ is the position vector at site i, and $\langle\cdots\rangle_i$ represents the expectation value at site i; in the following, the symbol $\tilde{X}$ represents the structure factor in terms of the multipole X. The orbital magnetic dipole operator M_μ is given by

$$M_x = \begin{pmatrix} 0 & 0 & 0 & 0 \\ 0 & 0 & 0 & 0 \\ 0 & 0 & 0 & -i \\ 0 & 0 & i & 0 \end{pmatrix}, \quad M_y = \begin{pmatrix} 0 & 0 & 0 & 0 \\ 0 & 0 & 0 & i \\ 0 & 0 & 0 & 0 \\ 0 & -i & 0 & 0 \end{pmatrix}, \quad M_z = \begin{pmatrix} 0 & 0 & 0 & 0 \\ 0 & 0 & -i & 0 \\ 0 & i & 0 & 0 \\ 0 & 0 & 0 & 0 \end{pmatrix}, \tag{4}$$

for the basis wave function $(\phi_0, \phi_x, \phi_y, \phi_z)$, where

$$\phi_0 = \frac{1}{\sqrt{4\pi}}, \quad \phi_x = \sqrt{\frac{3}{4\pi}}\frac{x}{r}, \quad \phi_y = \sqrt{\frac{3}{4\pi}}\frac{y}{r}, \quad \phi_z = \sqrt{\frac{3}{4\pi}}\frac{z}{r}. \tag{5}$$

We also define the structure factor of the total orbital magnetic dipole as $\tilde{M}(\boldsymbol{q}) = \sum_\mu \tilde{M}_\mu(\boldsymbol{q})$; this notation is consistently used for the different multipoles in the following discussions.

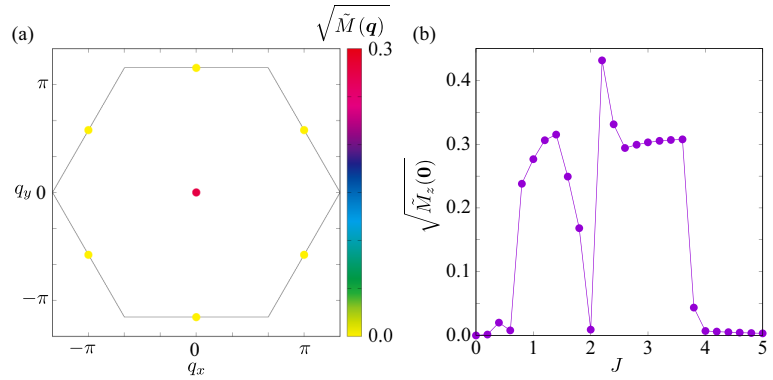

Figure 2. (a) Intensity plot of the structure factor in terms of the orbital magnetic dipole M at $\mu = -2$ and $J = 1$. (b) J dependence of the $\boldsymbol{q} = \boldsymbol{0}$ component of $\sqrt{\tilde{M}_z(\boldsymbol{q})}$.

 doi:10.20944/preprints202511.0660.v1

As shown in Figure 2(a), intensity maxima appear at the $\boldsymbol{q} = \boldsymbol{0}$ point in the Brillouin zone, while no significant intensity is observed at the M points. Among the components, only the z component of the orbital magnetic dipole, M_z, is finite. This behavior reflects the triple-Q nature of the four-sublattice chiral state, which possesses a uniform scalar spin chirality. The finite $\boldsymbol{q} = \boldsymbol{0}$ signal originates from circulating orbital currents induced by the noncoplanar spin configuration, where all triangular plaquettes share the same sign of chirality, forming a uniform orbital magnetic flux [106]. The appearance of a nonzero orbital magnetic dipole serves as the microscopic origin of the topological Hall effect even in the absence of relativistic spin–orbit coupling, since the orbital magnetic dipole directly couples to the Berry curvature that governs the Hall conductivity [40,107–113]. As shown in Figure 2(b), the uniform component remains finite across the entire range of J, indicating that the establishment of the triple-Q chiral order alone is sufficient to induce a uniform orbital angular momentum.

The persistence of $\boldsymbol{M}$ in the absence of spin–orbit coupling demonstrates that orbital magnetism can be generated purely from the scalar spin chirality, without any relativistic mechanism. This nonrelativistic orbital polarization provides a microscopic pathway toward anomalous Hall transport in chiral spin textures. Hence, the orbital magnetic dipole represents the lowest-rank manifestation of the coupling between itinerant electrons and noncoplanar spin textures, establishing a direct link between real-space chirality and momentum-space Berry curvature.

3.2. Spin and anisotropic magnetic dipoles

Figure 3(a,b) present the structure factors of the spin magnetic dipole $\boldsymbol{M}^{(\mathrm{s})}$ and the anisotropic magnetic dipole $\boldsymbol{M}_a^{(\mathrm{s})}$, respectively. Their operator definitions are given by [101]

$$\boldsymbol{M}^{(\mathrm{s})} = \begin{pmatrix} 1 & 0 & 0 & 0 \\ 0 & 1 & 0 & 0 \\ 0 & 0 & 1 & 0 \\ 0 & 0 & 0 & 1 \end{pmatrix} \boldsymbol{\sigma}, \tag{6}$$

$$M_{a,x}^{(\mathrm{s})} = \sqrt{\frac{3}{10}} \left(-\frac{1}{\sqrt{3}} Q_u^{(-)} \sigma_x + Q_{xy} \sigma_y + Q_{zx} \sigma_z \right), \tag{7}$$

$$M_{a,y}^{(\mathrm{s})} = \sqrt{\frac{3}{10}} \left(Q_{xy} \sigma_x - \frac{1}{\sqrt{3}} Q_u^{(+)} \sigma_y + Q_{yz} \sigma_z \right), \tag{8}$$

$$M_{a,z}^{(\mathrm{s})} = \sqrt{\frac{3}{10}} \left(Q_{zx} \sigma_x + Q_{yz} \sigma_y + \frac{2}{\sqrt{3}} Q_u \sigma_z \right), \tag{9}$$

where

$$Q_u = \frac{1}{5} \begin{pmatrix} 0 & 0 & 0 & 0 \\ 0 & -1 & 0 & 0 \\ 0 & 0 & -1 & 0 \\ 0 & 0 & 0 & 2 \end{pmatrix}, \quad Q_v = \frac{\sqrt{3}}{5} \begin{pmatrix} 0 & 0 & 0 & 0 \\ 0 & 1 & 0 & 0 \\ 0 & 0 & -1 & 0 \\ 0 & 0 & 0 & 0 \end{pmatrix},$$

$$Q_{yz} = \frac{\sqrt{3}}{5} \begin{pmatrix} 0 & 0 & 0 & 0 \\ 0 & 0 & 0 & 0 \\ 0 & 0 & 0 & 1 \\ 0 & 0 & 1 & 0 \end{pmatrix}, \quad Q_{zx} = \frac{\sqrt{3}}{5} \begin{pmatrix} 0 & 0 & 0 & 0 \\ 0 & 0 & 0 & 1 \\ 0 & 0 & 0 & 0 \\ 0 & 1 & 0 & 0 \end{pmatrix},$$

$$Q_{xy} = \frac{\sqrt{3}}{5} \begin{pmatrix} 0 & 0 & 0 & 0 \\ 0 & 0 & 1 & 0 \\ 0 & 1 & 0 & 0 \\ 0 & 0 & 0 & 0 \end{pmatrix}, \tag{10}$$

 doi:10.20944/preprints202511.0660.v1

with $Q_u^{(\pm)} = Q_u \pm \sqrt{3}Q_v$ and $Q_v^{(\pm)} = \pm\sqrt{3}Q_u + Q_v$. The former spin magnetic dipole is related to the spin contribution of the magnetic moments, while the latter anisotropic magnetic dipole is related to the onset of the anomalous Hall effect in antiferromagnets and is referred to as the $\boldsymbol{T}$ vector in the context of X-ray magnetic circular dichroism measurements [114–118].

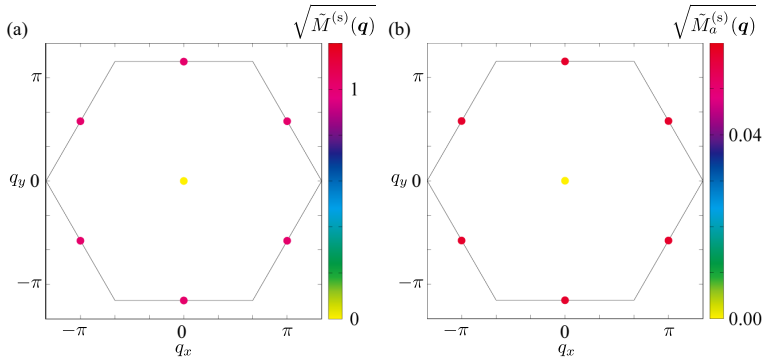

Figure 3. Intensity plots of the structure factor in terms of (a) the spin magnetic dipole $M^{(s)}$ and (b) the anisotropic magnetic dipole $M_a^{(s)}$ at $\mu = -2$ and $J = 1$.

In Figure 3(a), the intensity distribution of $\boldsymbol{M}^{(s)}$ exhibits peaks at the M points in the Brillouin zone, while no clear signal appears at $\boldsymbol{q} = \boldsymbol{0}$. This behavior indicates that the modulation of the spin magnetic moments directly follows the four-sublattice periodicity of the triple-Q chiral structure, and there is no net spin magnetization in the system. In real space, the corresponding distribution shown in Figure 4(a) reveals that the spin magnetic dipoles on the four sublattices are oriented toward the vertices of a regular tetrahedron. This noncoplanar spin configuration leads to a uniform scalar spin chirality, $\chi_{ijk} = \boldsymbol{M}_i^{(s)} \cdot (\boldsymbol{M}_j^{(s)} \times \boldsymbol{M}_k^{(s)})$, which acts as an emergent magnetic field for the itinerant electrons without the net spin magnetization, as found by the peak structure of the orbital magnetic dipole $\boldsymbol{M}$ at the $\boldsymbol{q} = \boldsymbol{0}$ component.

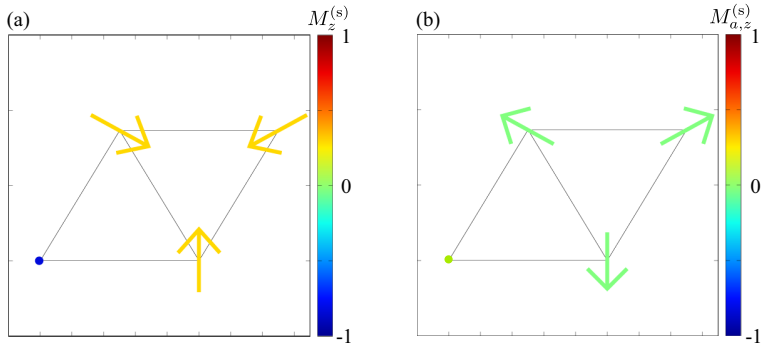

Figure 4. Real-space plots of (a) the spin magnetic dipole $\boldsymbol{M}^{(s)} = (M_x^{(s)}, M_y^{(s)}, M_z^{(s)})$ and (b) the anisotropic magnetic dipole $\boldsymbol{M}_a^{(s)} = (M_{a,x}^{(s)}, M_{a,y}^{(s)}, M_{a,z}^{(s)})$ at $\mu = -2$ and $J = 1$. The color represents the z component.

The behavior of the anisotropic magnetic dipole $\boldsymbol{M}_a^{(s)}$ shown in Figures 3(b) and 4(b) closely resembles that of the spin magnetic dipole $\boldsymbol{M}^{(s)}$. As seen in Figure 3(b), the intensity distribution of $\boldsymbol{M}_a^{(s)}$ exhibits peaks at the M points in the Brillouin zone, similar to $\boldsymbol{M}^{(s)}$ in Figure 3(a). This correspondence indicates that both isotropic spin and anisotropic magnetic dipoles share the same four-sublattice periodicity originating from the triple-Q chiral order. The real-space distribution in Figure 4(b) also shows a spatial pattern similar to that of $\boldsymbol{M}^{(s)}$ in Figure 4(a), with the amplitude of $\boldsymbol{M}_a^{(s)}$ modulating periodically within the magnetic unit cell. This similarity between $\boldsymbol{M}^{(s)}$ and $\boldsymbol{M}_a^{(s)}$ suggests that the anisotropic magnetic dipole originates from the same underlying chiral spin geometry.

 doi:10.20944/preprints202511.0660.v1

3.3. Effective Spin–Orbit Coupling

We next analyze the behavior of the spin-dependent electric monopole $Q_0^{(s)}$, which represents the lowest-rank even-parity electric multipole induced by the interplay between the spin texture and charge degrees of freedom. The definition of the operator $Q_0^{(s)}$ is given by

$$Q_0^{(s)} = \frac{1}{\sqrt{3}}(M_x\sigma_x + M_y\sigma_y + M_z\sigma_z). \tag{11}$$

Thus, the spin-dependent electric monopole is described by the inner product of the orbital magnetic dipole and the Pauli matrix, which is proportional to the atomic spin–orbit coupling.

As shown in Figure 5(a), the structure factor of $Q_0^{(s)}$ exhibits peaks at the M points in the Brillouin zone, while no intensity appears at $\boldsymbol{q} = \boldsymbol{0}$. This feature indicates that the modulation of $Q_0^{(s)}$ follows the four-sublattice periodicity of the triple-Q chiral magnetic structure. The M-point peaks arise from the alternating sign of the local monopole moment among neighboring sites, reflecting the spatial variation of the spin canting angles in the noncoplanar configuration. Hence, the resulting $Q_0^{(s)}$ does not possess a uniform component but instead exhibits a periodic modulation synchronized with the chiral spin texture.

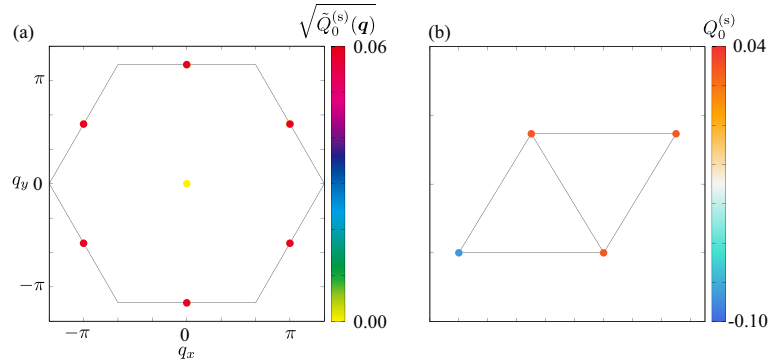

Figure 5. (a) Intensity plot of the structure factor in terms of the spin-dependent electric monopole $Q_0^{(s)}$ at $\mu = -2$ and $J = 1$. (b) Corresponding real-space plot.

The corresponding real-space distribution in Figure 5(b) shows that the monopole amplitude alternates in sign across the four sublattices, forming a pattern consistent with the underlying scalar spin chirality. Such behavior demonstrates that the noncoplanar spin arrangement acts as an internal source of sublattice-dependent spin–orbital entanglement, even in the absence of relativistic spin–orbit coupling. The emergence of this staggered monopolar quantity provides a microscopic mechanism for the inner-product coupling between the spin and charge sectors via exchange-driven hybridization effects.

3.4. Axial Density Waves

Finally, we show that the four-sublattice chiral spin texture on the triangular lattice also exhibits the density wave in terms of the unconventional ferroaxial moments. The ferroaxial moment represents an axial vector order parameter that characterizes a spontaneous rotation of the crystal structure, and belongs to the same symmetry class as the electric toroidal dipole [119–122]. In general, the electric toroidal dipole can emerge in systems where spatial inversion and time-reversal symmetries are both preserved, leading to off-diagonal cross-correlation responses [87,123,124], such as the antisymmetric thermopolarization [125], intrinsic longitudinal spin current generation [87,126], and transverse nonlinear magnetic response [127]. Recent spectroscopic investigations have revealed ferroic ordering of electric toroidal dipoles in a variety of materials. Such ferroaxial orderings have been experimentally identified in several crystalline systems, including $RbFe(MoO_4)_2$ [128,129], $NiTiO_3$ [129–131],

 doi:10.20944/preprints202511.0660.v1

$Ca_5Ir_3O_{12}$ [132–135], and $BaCoSiO_4$ [136]. These studies have established ferroaxiality as a distinct type of ferroic order, characterized by the uniform alignment of the electric toroidal dipole.

In our system, the ferroaxial moment is described by the spatial pattern of the spin-dependent electric toroidal dipole $\boldsymbol{G}^{(\mathrm{s})}$, whose expression is given by the vector product between the orbital magnetic dipole and the Pauli matrix as

$$\boldsymbol{G}^{(\mathrm{s})} = \frac{1}{\sqrt{2}}(\boldsymbol{\sigma} \times \boldsymbol{M}). \tag{12}$$

As shown in Figure 5(a), the structure factor of $\boldsymbol{G}^{(\mathrm{s})}$ exhibits pronounced peaks at the M points in the Brillouin zone, following the four-sublattice periodicity of the triple-Q chiral magnetic order. Meanwhile, there is no intensity at $\boldsymbol{q} = \boldsymbol{0}$, meaning no its uniform component. The corresponding real-space distribution in Figure 5(b) displays a loop-like circulation of local electric toroidal dipole vectors around the triangular plaquette consisting of sublattices B, C, and D, which also indicates no net electric toroidal dipole moment in the whole system.

The local ferroaxial moment in the present system does not originate from any lattice rotation or structural distortion, as observed in conventional ferroaxial materials [137]. Instead, it arises purely from the noncoplanar magnetic structure, which leads to a mirror symmetry breaking at sublattices B–D. This purely magnetic origin demonstrates that chiral spin configurations can mimic ferroaxial behavior without invoking atomic displacements.

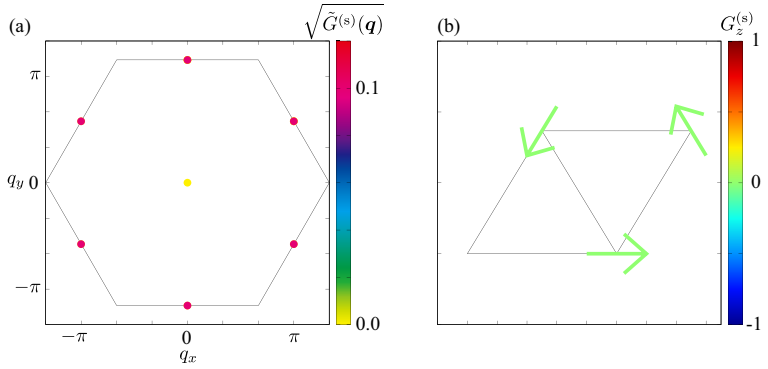

Figure 6. (a) Intensity plot of the structure factor in terms of the spin-dependent electric toroidal dipole $G^{(\mathrm{s})}$ at $\mu = -2$ and $J = 1$. (b) Corresponding real-space plot, where the arrows represent the direction of the electric toroidal dipole.

4. Results with the Spin–Orbit Coupling

We next investigate how the atomic spin–orbit coupling modifies the multipole responses under the four-sublattice chiral magnetic order by setting $\lambda = 0.5$. Figures 7(a)–(e) show the calculated structure factors of five representative quantities: (a) the orbital magnetic dipole $\boldsymbol{M}$, (b) the spin magnetic dipole $\boldsymbol{M}^{(\mathrm{s})}$, (c) the anisotropic magnetic dipole $\boldsymbol{M}_a^{(\mathrm{s})}$, (d) the spin-dependent electric monopole $Q_0^{(\mathrm{s})}$, and (e) the spin-dependent electric toroidal dipole $\boldsymbol{G}^{(\mathrm{s})}$. Compared with the case without spin–orbit coupling, where most multipoles except for $\boldsymbol{M}$ exhibit intensity maxima at the M points, the inclusion of the spin–orbit coupling selectively activates uniform ($\boldsymbol{q} = \boldsymbol{0}$) components while keeping others modulated at the M points.

In Figure 7(a), the orbital magnetic dipole $\boldsymbol{M}$ maintains its peak at $\boldsymbol{q} = \boldsymbol{0}$, indicating that its uniform nature is predominantly governed by the underlying chiral orbital currents and is only weakly affected by the spin–orbit coupling. In contrast, the spin magnetic dipole $\boldsymbol{M}^{(\mathrm{s})}$ in Figure 7(b) develops an additional $\boldsymbol{q} = \boldsymbol{0}$ component, which was absent in the spin-orbit-coupling-free case. This new uniform intensity indicates that λ couples the spin and orbital sectors, transferring part of the uniform modulation of the orbital magnetic dipole into the spin magnetic dipole. Conversely, the spin magnetic dipole components at the M points are transferred into orbital magnetic dipole moments at the M

Preprints.org (www.preprints.org) | NOT PEER-REVIEWED | Posted: 10 November 2025 doi:10.20944/preprints202511.0660.v1

point. A similar effect appears for the anisotropic magnetic dipole $\boldsymbol{M}_a^{(\mathrm{s})}$ in Figure 7(c), where the purely M-point modulation seen without spin-orbit coupling evolves into a mixed pattern containing a weak but finite $\boldsymbol{q} = \boldsymbol{0}$ signal.

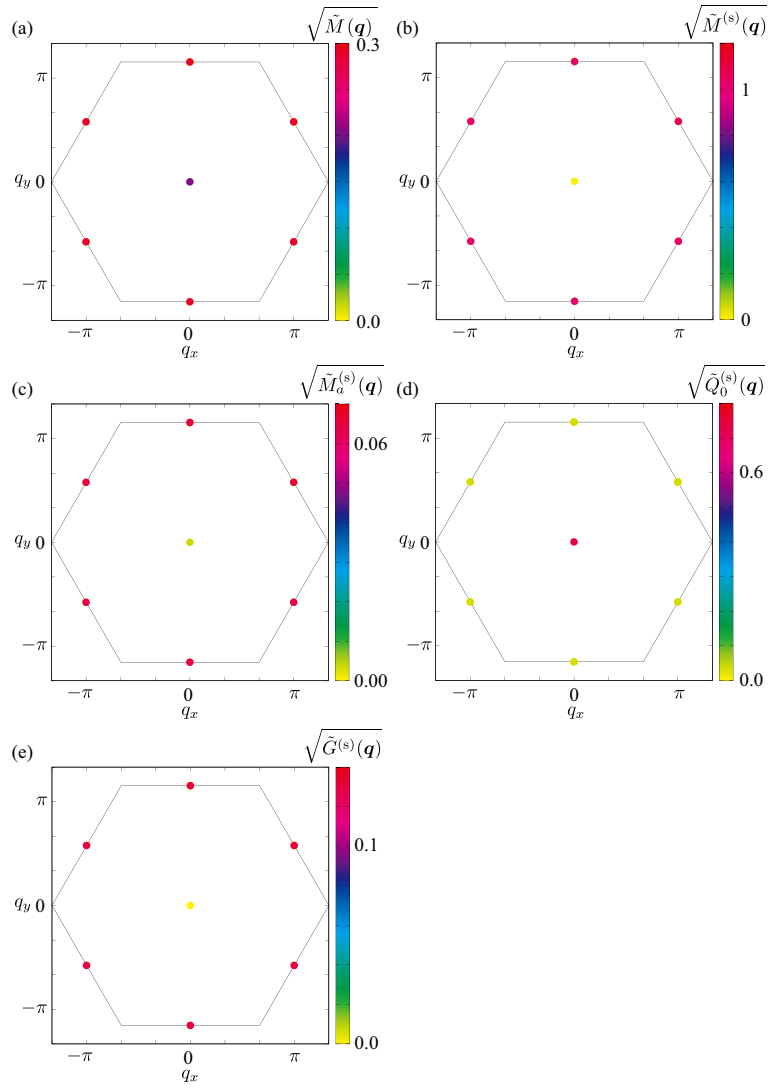

Figure 7. Intensity plots of the structure factor in terms of (a) the orbital magnetic dipole M, (b) the spin magnetic dipole $M^{(\mathrm{s})}$, (c) the anisotropic magnetic dipole $M_a^{(\mathrm{s})}$, (d) the spin-dependent electric monopole $Q_0^{(\mathrm{s})}$, and (e) the spin-dependent electric toroidal dipole $G^{(\mathrm{s})}$ at $\mu = -2$, $J = 1$, and $\lambda = 0.5$.

For the spin-dependent electric monopole $Q_0^{(\mathrm{s})}$ shown in Figure 7(d), the spectral weight remains at the M points as in the spin-orbit-coupling-free case, but a uniform component emerges, reflecting the introduction of the relativistic spin–orbit coupling. On the other hand, the spin-dependent electric toroidal dipole $\boldsymbol{G}^{(\mathrm{s})}$ in Figure 7(e) retains its characteristic M-point peaks, whereas no uniform peak structure appears. This implies that the ferroaxial character manifests only locally, while its net macroscopic contribution cancels out even with the spin–orbit coupling.

These results collectively reveal that the spin–orbit coupling functions as a selective mediator among the multipole channels. It enhances the uniform ($\boldsymbol{q} = \boldsymbol{0}$) components of the dipolar and monopolar multipoles through the hybridization between spin and orbital degrees of freedom, while the electric toroidal dipole channel remains predominantly modulated at the M points. Such a selective activation of uniform responses reflects the symmetry-allowed nature of the relativistic coupling under the magnetic point group rather than the spin point group.

 doi:10.20944/preprints202511.0660.v1

5. Conclusions

We have presented a unified microscopic framework for emergent multipoles in a four-sublattice chiral state on a triangular lattice, clarifying how the noncoplanar spin texture generates characteristic momentum- and real-space features and how the atomic spin–orbit coupling modifies them. In the absence of spin–orbit coupling, the orbital magnetic dipole exhibits a uniform $\boldsymbol{q} = \boldsymbol{0}$ component originating from circulating orbital currents tied to the scalar spin chirality, whereas the spin magnetic dipole, anisotropic magnetic dipole, spin-dependent electric monopole, and spin-dependent electric toroidal dipole display distinct M-point modulations reflecting the four-sublattice periodicity. Once the spin–orbit coupling is introduced, uniform spectral weight appears selectively in several channels—most notably in the spin and anisotropic magnetic dipoles and in the spin-dependent electric monopole—while the spin-dependent electric toroidal dipole remains predominantly finite-q-modulated. This selective activation demonstrates that the spin–orbit coupling mediates symmetry-allowed mixing among spin, charge, and orbital sectors, which plays a different role from the noncoplanar-order-driven mixing. The present framework provides perspectives for extending this study to other frustrated magnetic systems and for guiding experimental realizations. The same multipole hierarchy is expected to manifest in other geometrically frustrated lattices, such as kagome, face-centered-cubic, and pyrochlore systems, where noncoplanar multiple-Q spin states are stabilized by competing exchanges, higher-order spin interactions, or Fermi-surface nesting.

Funding: This research was supported by JSPS KAKENHI Grants Numbers JP22H00101, JP22H01183, JP23H04869, JP23K03288, JP23K20827, and by JST CREST (JPMJCR23O4) and JST FOREST (JPMJFR2366).

Data Availability Statement: The original contributions presented in the study are included in the article, further inquiries can be directed to the corresponding author.

References

1. Ohgushi, K.; Murakami, S.; Nagaosa, N. Spin anisotropy and quantum Hall effect in the *kagomé* lattice: Chiral spin state based on a ferromagnet. *Phys. Rev. B* **2000**, *62*, R6065–R6068. https://doi.org/10.1103/PhysRevB.62.R6065.
2. Taguchi, Y.; Oohara, Y.; Yoshizawa, H.; Nagaosa, N.; Tokura, Y. Spin chirality, Berry phase, and anomalous Hall effect in a frustrated ferromagnet. *Science* **2001**, *291*, 2573–2576. https://doi.org/10.1126/science.1058161.
3. Tatara, G.; Kawamura, H. Chirality-driven anomalous Hall effect in weak coupling regime. *J. Phys. Soc. Jpn.* **2002**, *71*, 2613–2616. https://doi.org/10.1143/JPSJ.71.2613.
4. Binz, B.; Vishwanath, A. Theory of helical spin crystals: Phases, textures, and properties. *Phys. Rev. B* **2006**, *74*, 214408. https://doi.org/10.1103/PhysRevB.74.214408.
5. Machida, Y.; Nakatsuji, S.; Maeno, Y.; Tayama, T.; Sakakibara, T.; Onoda, S. Unconventional anomalous Hall effect enhanced by a noncoplanar spin texture in the frustrated Kondo lattice $Pr_2Ir_2O_7$. *Phys. Rev. Lett.* **2007**, *98*, 057203. https://doi.org/10.1103/PhysRevLett.98.057203.
6. Neubauer, A.; Pfleiderer, C.; Binz, B.; Rosch, A.; Ritz, R.; Niklowitz, P.G.; Böni, P. Topological Hall Effect in the *A* Phase of MnSi. *Phys. Rev. Lett.* **2009**, *102*, 186602. https://doi.org/10.1103/PhysRevLett.102.186602.
7. Nagaosa, N.; Tokura, Y. Topological properties and dynamics of magnetic skyrmions. *Nat. Nanotechnol.* **2013**, *8*, 899–911. https://doi.org/10.1038/nnano.2013.243.
8. Tokura, Y.; Nagaosa, N. Nonreciprocal responses from non-centrosymmetric quantum materials. *Nat. Commun.* **2018**, *9*, 3740. https://doi.org/10.1038/s41467-018-05759-4.
9. Hayami, S.; Okubo, T.; Motome, Y. Phase shift in skyrmion crystals. *Nat. Commun.* **2021**, *12*, 6927. https://doi.org/10.1038/s41467-021-27083-0.
10. Hayami, S.; Yatsushiro, M. Nonlinear nonreciprocal transport in antiferromagnets free from spin-orbit coupling. *Phys. Rev. B* **2022**, *106*, 014420. https://doi.org/10.1103/PhysRevB.106.014420.
11. Hayami, S.; Yatsushiro, M. Nonreciprocal Transport in Noncoplanar Magnetic Systems without Spin–Orbit Coupling, Net Scalar Chirality, or Magnetization. *J. Phys. Soc. Jpn.* **2022**, *91*, 094704. https://doi.org/10.7566/JPSJ.91.094704.

 doi:10.20944/preprints202511.0660.v1

12. Eto, R.; Pohle, R.; Mochizuki, M. Low-Energy Excitations of Skyrmion Crystals in a Centrosymmetric Kondo-Lattice Magnet: Decoupled Spin-Charge Excitations and Nonreciprocity. *Phys. Rev. Lett.* **2022**, *129*, 017201. https://doi.org/10.1103/PhysRevLett.129.017201.
13. Olive, J.A.; Young, A.P.; Sherrington, D. Computer simulation of the three-dimensional short-range Heisenberg spin glass. *Phys. Rev. B* **1986**, *34*, 6341–6346. https://doi.org/10.1103/PhysRevB.34.6341.
14. Kawamura, H. Chiral ordering in Heisenberg spin glasses in two and three dimensions. *Phys. Rev. Lett.* **1992**, *68*, 3785–3788. https://doi.org/10.1103/PhysRevLett.68.3785.
15. Hayami, S.; Yambe, R. Stabilization mechanisms of magnetic skyrmion crystal and multiple-Q states based on momentum-resolved spin interactions. *Mater. Today Quantum* **2024**, *3*, 100010. https://doi.org/https://doi.org/10.1016/j.mtquan.2024.100010.
16. Kawamura, H. Frustration-induced skyrmion crystals in centrosymmetric magnets. *J. Phys.: Condens. Matter* **2025**, *37*, 183004. https://doi.org/10.1088/1361-648X/adbf5b.
17. Martin, I.; Batista, C.D. Itinerant Electron-Driven Chiral Magnetic Ordering and Spontaneous Quantum Hall Effect in Triangular Lattice Models. *Phys. Rev. Lett.* **2008**, *101*, 156402. https://doi.org/10.1103/PhysRevLett.101.156402.
18. Akagi, Y.; Motome, Y. Spin Chirality Ordering and Anomalous Hall Effect in the Ferromagnetic Kondo Lattice Model on a Triangular Lattice. *J. Phys. Soc. Jpn.* **2010**, *79*, 083711. https://doi.org/10.1143/JPSJ.79.083711.
19. Kumar, S.; van den Brink, J. Frustration-Induced Insulating Chiral Spin State in Itinerant Triangular-Lattice Magnets. *Phys. Rev. Lett.* **2010**, *105*, 216405. https://doi.org/10.1103/PhysRevLett.105.216405.
20. Kato, Y.; Martin, I.; Batista, C.D. Stability of the Spontaneous Quantum Hall State in the Triangular Kondo-Lattice Model. *Phys. Rev. Lett.* **2010**, *105*, 266405. https://doi.org/10.1103/PhysRevLett.105.266405.
21. Bak, P.; Lebech, B. "Triple-$\vec{q}$" Modulated Magnetic Structure and Critical Behavior of Neodymium. *Phys. Rev. Lett.* **1978**, *40*, 800–803. https://doi.org/10.1103/PhysRevLett.40.800.
22. McEwen, K.A.; Walker, M.B. Free-energy analysis of the single-q and double-q magnetic structures of neodymium. *Phys. Rev. B* **1986**, *34*, 1781–1783. https://doi.org/10.1103/PhysRevB.34.1781.
23. Zochowski, S.; McEwen, K. Thermal expansion study of the magnetic phase diagram of neodymium. *J. Magn. Magn. Mater.* **1986**, *54*, 515–516. https://doi.org/https://doi.org/10.1016/0304-8853(86)90688-8.
24. Forgan, E.; Rainford, B.; Lee, S.; Abell, J.; Bi, Y. The magnetic structure of $CeAl_2$ is a non-chiral spiral. *J. Phys.: Condens. Matter* **1990**, *2*, 10211.
25. Korshunov, S.E. Chiral phase of the Heisenberg antiferromagnet with a triangular lattice. *Phys. Rev. B* **1993**, *47*, 6165–6168. https://doi.org/10.1103/PhysRevB.47.6165.
26. Messio, L.; Lhuillier, C.; Misguich, G. Lattice symmetries and regular magnetic orders in classical frustrated antiferromagnets. *Phys. Rev. B* **2011**, *83*, 184401. https://doi.org/10.1103/PhysRevB.83.184401.
27. Kurz, P.; Bihlmayer, G.; Hirai, K.; Blügel, S. Three-Dimensional Spin Structure on a Two-Dimensional Lattice: Mn/Cu(111). *Phys. Rev. Lett.* **2001**, *86*, 1106–1109. https://doi.org/10.1103/PhysRevLett.86.1106.
28. Gong, S.S.; Zhu, W.; Zhu, J.X.; Sheng, D.N.; Yang, K. Global phase diagram and quantum spin liquids in a spin-$\frac{1}{2}$ triangular antiferromagnet. *Phys. Rev. B* **2017**, *96*, 075116. https://doi.org/10.1103/PhysRevB.96.075116.
29. Barros, K.; Venderbos, J.W.F.; Chern, G.W.; Batista, C.D. Exotic magnetic orderings in the kagome Kondo-lattice model. *Phys. Rev. B* **2014**, *90*, 245119. https://doi.org/10.1103/PhysRevB.90.245119.
30. Ghosh, S.; O'Brien, P.; Henley, C.L.; Lawler, M.J. Phase diagram of the Kondo lattice model on the kagome lattice. *Phys. Rev. B* **2016**, *93*, 024401. https://doi.org/10.1103/PhysRevB.93.024401.
31. Shindou, R.; Nagaosa, N. Orbital Ferromagnetism and Anomalous Hall Effect in Antiferromagnets on the Distorted fcc Lattice. *Phys. Rev. Lett.* **2001**, *87*, 116801. https://doi.org/10.1103/PhysRevLett.87.116801.
32. Balla, P.; Iqbal, Y.; Penc, K. Degenerate manifolds, helimagnets, and multi-Q chiral phases in the classical Heisenberg antiferromagnet on the face-centered-cubic lattice. *Phys. Rev. Research* **2020**, *2*, 043278. https://doi.org/10.1103/PhysRevResearch.2.043278.
33. Momoi, T.; Kubo, K.; Niki, K. Possible Chiral Phase Transition in Two-Dimensional Solid ^{3}He. *Phys. Rev. Lett.* **1997**, *79*, 2081–2084. https://doi.org/10.1103/PhysRevLett.79.2081.
34. Akagi, Y.; Udagawa, M.; Motome, Y. Hidden Multiple-Spin Interactions as an Origin of Spin Scalar Chiral Order in Frustrated Kondo Lattice Models. *Phys. Rev. Lett.* **2012**, *108*, 096401. https://doi.org/10.1103/PhysRevLett.108.096401.
35. Kato, Y.; Ishizuka, H. Colossal Enhancement of Spin-Chirality-Related Hall Effect by Thermal Fluctuation. *Phys. Rev. Appl.* **2019**, *12*, 021001. https://doi.org/10.1103/PhysRevApplied.12.021001.

 doi:10.20944/preprints202511.0660.v1

36. Berry, M.V. Quantal phase factors accompanying adiabatic changes. *Proceedings of the Royal Society of London A: Mathematical, Physical and Engineering Sciences* **1984**, *392*, 45–57. https://doi.org/10.1098/rspa.1984.0023.
37. Loss, D.; Goldbart, P.M. Persistent currents from Berry's phase in mesoscopic systems. *Phys. Rev. B* **1992**, *45*, 13544–13561. https://doi.org/10.1103/PhysRevB.45.13544.
38. Ye, J.; Kim, Y.B.; Millis, A.J.; Shraiman, B.I.; Majumdar, P.; Tešanović, Z. Berry Phase Theory of the Anomalous Hall Effect: Application to Colossal Magnetoresistance Manganites. *Phys. Rev. Lett.* **1999**, *83*, 3737–3740. https://doi.org/10.1103/PhysRevLett.83.3737.
39. Nagaosa, N.; Sinova, J.; Onoda, S.; MacDonald, A.H.; Ong, N.P. Anomalous Hall effect. *Rev. Mod. Phys.* **2010**, *82*, 1539–1592. https://doi.org/10.1103/RevModPhys.82.1539.
40. Xiao, D.; Chang, M.C.; Niu, Q. Berry phase effects on electronic properties. *Rev. Mod. Phys.* **2010**, *82*, 1959–2007. https://doi.org/10.1103/RevModPhys.82.1959.
41. Bogdanov, A.N.; Yablonskii, D.A. Thermodynamically stable "vortices" in magnetically ordered crystals: The mixed state of magnets. *Sov. Phys. JETP* **1989**, *68*, 101.
42. Bogdanov, A.; Hubert, A. Thermodynamically stable magnetic vortex states in magnetic crystals. *J. Magn. Magn. Mater.* **1994**, *138*, 255 – 269. https://doi.org/http://dx.doi.org/10.1016/0304-8853(94)90046-9.
43. Rößler, U.K.; Bogdanov, A.N.; Pfleiderer, C. Spontaneous skyrmion ground states in magnetic metals. *Nature* **2006**, *442*, 797–801. https://doi.org/10.1038/nature05056.
44. Mühlbauer, S.; Binz, B.; Jonietz, F.; Pfleiderer, C.; Rosch, A.; Neubauer, A.; Georgii, R.; Böni, P. Skyrmion lattice in a chiral magnet. *Science* **2009**, *323*, 915–919. https://doi.org/10.1126/science.1166767.
45. Jonietz, F.; Mühlbauer, S.; Pfleiderer, C.; Neubauer, A.; Münzer, W.; Bauer, A.; Adams, T.; Georgii, R.; Böni, P.; Duine, R.A.; et al. Spin Transfer Torques in MnSi at Ultralow Current Densities. *Science* **2010**, *330*, 1648. https://doi.org/10.1126/science.1195709.
46. Adams, T.; Mühlbauer, S.; Pfleiderer, C.; Jonietz, F.; Bauer, A.; Neubauer, A.; Georgii, R.; Böni, P.; Keiderling, U.; Everschor, K.; et al. Long-Range Crystalline Nature of the Skyrmion Lattice in MnSi. *Phys. Rev. Lett.* **2011**, *107*, 217206. https://doi.org/10.1103/PhysRevLett.107.217206.
47. Bauer, A.; Pfleiderer, C. Magnetic phase diagram of MnSi inferred from magnetization and ac susceptibility. *Phys. Rev. B* **2012**, *85*, 214418. https://doi.org/10.1103/PhysRevB.85.214418.
48. Bauer, A.; Garst, M.; Pfleiderer, C. Specific Heat of the Skyrmion Lattice Phase and Field-Induced Tricritical Point in MnSi. *Phys. Rev. Lett.* **2013**, *110*, 177207. https://doi.org/10.1103/PhysRevLett.110.177207.
49. Chacon, A.; Bauer, A.; Adams, T.; Rucker, F.; Brandl, G.; Georgii, R.; Garst, M.; Pfleiderer, C. Uniaxial Pressure Dependence of Magnetic Order in MnSi. *Phys. Rev. Lett.* **2015**, *115*, 267202. https://doi.org/10.1103/PhysRevLett.115.267202.
50. Mühlbauer, S.; Kindervater, J.; Adams, T.; Bauer, A.; Keiderling, U.; Pfleiderer, C. Kinetic small angle neutron scattering of the skyrmion lattice in MnSi. *New J. Phys.* **2016**, *18*, 075017. https://doi.org/10.1088/1367-2630/18/7/075017.
51. Reiner, M.; Bauer, A.; Leitner, M.; Gigl, T.; Anwand, W.; Butterling, M.; Wagner, A.; Kudejova, P.; Pfleiderer, C.; Hugenschmidt, C. Positron spectroscopy of point defects in the skyrmion-lattice compound MnSi. *Sci. Rep.* **2016**, *6*, 29109. https://doi.org/https://doi.org/10.1038/srep29109.
52. Yu, X.Z.; Onose, Y.; Kanazawa, N.; Park, J.H.; Han, J.H.; Matsui, Y.; Nagaosa, N.; Tokura, Y. Real-space observation of a two-dimensional skyrmion crystal. *Nature* **2010**, *465*, 901–904. https://doi.org/10.1038/nature09124.
53. Münzer, W.; Neubauer, A.; Adams, T.; Mühlbauer, S.; Franz, C.; Jonietz, F.; Georgii, R.; Böni, P.; Pedersen, B.; Schmidt, M.; et al. Skyrmion lattice in the doped semiconductor $Fe_{1-x}Co_xSi$. *Phys. Rev. B* **2010**, *81*, 041203. https://doi.org/10.1103/PhysRevB.81.041203.
54. Adams, T.; Mühlbauer, S.; Neubauer, A.; Münzer, W.; Jonietz, F.; Georgii, R.; Pedersen, B.; Böni, P.; Rosch, A.; Pfleiderer, C. Skyrmion lattice domains in $Fe_{1-x}Co_xSi$. In Proceedings of the J. Phys.: Conf. Ser. IOP Publishing, 2010, Vol. 200, p. 032001. https://doi.org/10.1088/1742-6596/200/3/032001.
55. Yu, X.Z.; Kanazawa, N.; Onose, Y.; Kimoto, K.; Zhang, W.; Ishiwata, S.; Matsui, Y.; Tokura, Y. Near room-temperature formation of a skyrmion crystal in thin-films of the helimagnet FeGe. *Nat. Mater.* **2011**, *10*, 106–109. https://doi.org/10.1038/nmat2916.
56. Gallagher, J.C.; Meng, K.Y.; Brangham, J.T.; Wang, H.L.; Esser, B.D.; McComb, D.W.; Yang, F.Y. Robust Zero-Field Skyrmion Formation in FeGe Epitaxial Thin Films. *Phys. Rev. Lett.* **2017**, *118*, 027201. https://doi.org/10.1103/PhysRevLett.118.027201.

 doi:10.20944/preprints202511.0660.v1

57. Turgut, E.; Paik, H.; Nguyen, K.; Muller, D.A.; Schlom, D.G.; Fuchs, G.D. Engineering Dzyaloshinskii-Moriya interaction in B20 thin-film chiral magnets. *Phys. Rev. Mater.* **2018**, *2*, 074404. https://doi.org/10.1103/PhysRevMaterials.2.074404.
58. Spencer, C.S.; Gayles, J.; Porter, N.A.; Sugimoto, S.; Aslam, Z.; Kinane, C.J.; Charlton, T.R.; Freimuth, F.; Chadov, S.; Langridge, S.; et al. Helical magnetic structure and the anomalous and topological Hall effects in epitaxial B20 $Fe_{1-y}Co_yGe$ films. *Phys. Rev. B* **2018**, *97*, 214406. https://doi.org/10.1103/PhysRevB.97.214406.
59. Kakihana, M.; Aoki, D.; Nakamura, A.; Honda, F.; Nakashima, M.; Amako, Y.; Nakamura, S.; Sakakibara, T.; Hedo, M.; Nakama, T.; et al. Giant Hall resistivity and magnetoresistance in cubic chiral antiferromagnet EuPtSi. *J. Phys. Soc. Jpn.* **2018**, *87*, 023701. https://doi.org/10.7566/JPSJ.87.023701.
60. Kaneko, K.; Frontzek, M.D.; Matsuda, M.; Nakao, A.; Munakata, K.; Ohhara, T.; Kakihana, M.; Haga, Y.; Hedo, M.; Nakama, T.; et al. Unique Helical Magnetic Order and Field-Induced Phase in Trillium Lattice Antiferromagnet EuPtSi. *J. Phys. Soc. Jpn.* **2019**, *88*, 013702. https://doi.org/10.7566/JPSJ.88.013702.
61. Tabata, C.; Matsumura, T.; Nakao, H.; Michimura, S.; Kakihana, M.; Inami, T.; Kaneko, K.; Hedo, M.; Nakama, T.; Ōnuki, Y. Magnetic Field Induced Triple-q Magnetic Order in Trillium Lattice Antiferromagnet EuPtSi Studied by Resonant X-ray Scattering. *J. Phys. Soc. Jpn.* **2019**, *88*, 093704. https://doi.org/10.7566/JPSJ.88.093704.
62. Kakihana, M.; Aoki, D.; Nakamura, A.; Honda, F.; Nakashima, M.; Amako, Y.; Takeuchi, T.; Harima, H.; Hedo, M.; Nakama, T.; et al. Unique Magnetic Phases in the Skyrmion Lattice and Fermi Surface Properties in Cubic Chiral Antiferromagnet EuPtSi. *J. Phys. Soc. Jpn.* **2019**, *88*, 094705. https://doi.org/10.7566/JPSJ.88.094705.
63. Balasubramanian, B.; Manchanda, P.; Pahari, R.; Chen, Z.; Zhang, W.; Valloppilly, S.R.; Li, X.; Sarella, A.; Yue, L.; Ullah, A.; et al. Chiral Magnetism and High-Temperature Skyrmions in B20-Ordered Co-Si. *Phys. Rev. Lett.* **2020**, *124*, 057201. https://doi.org/10.1103/PhysRevLett.124.057201.
64. Hayami, S.; Yambe, R. Field-Direction Sensitive Skyrmion Crystals in Cubic Chiral Systems: Implication to $4f$-Electron Compound EuPtSi. *J. Phys. Soc. Jpn.* **2021**, *90*, 073705. https://doi.org/10.7566/JPSJ.90.073705.
65. Borisov, V.; Xu, Q.; Ntallis, N.; Clulow, R.; Shtender, V.; Cedervall, J.; Sahlberg, M.; Wikfeldt, K.T.; Thonig, D.; Pereiro, M.; et al. Tuning skyrmions in B20 compounds by 4d and 5d doping. *Phys. Rev. Mater.* **2022**, *6*, 084401. https://doi.org/10.1103/PhysRevMaterials.6.084401.
66. Kézsmárki, I.; Bordács, S.; Milde, P.; Neuber, E.; Eng, L.M.; White, J.S.; Rønnow, H.M.; Dewhurst, C.D.; Mochizuki, M.; Yanai, K.; et al. Neel-type skyrmion lattice with confined orientation in the polar magnetic semiconductor GaV_4S_8. *Nat. Mater.* **2015**, *14*, 1116–1122. https://doi.org/10.1038/nmat4402.
67. Bordács, S.; Butykai, A.; Szigeti, B.G.; White, J.S.; Cubitt, R.; Leonov, A.O.; Widmann, S.; Ehlers, D.; von Nidda, H.A.K.; Tsurkan, V.; et al. Equilibrium skyrmion lattice ground state in a polar easy-plane magnet. *Sci. Rep.* **2017**, *7*, 7584. https://doi.org/10.1038/s41598-017-07996-x.
68. Fujima, Y.; Abe, N.; Tokunaga, Y.; Arima, T. Thermodynamically stable skyrmion lattice at low temperatures in a bulk crystal of lacunar spinel GaV_4Se_8. *Phys. Rev. B* **2017**, *95*, 180410. https://doi.org/10.1103/PhysRevB.95.180410.
69. Kurumaji, T.; Nakajima, T.; Ukleev, V.; Feoktystov, A.; Arima, T.h.; Kakurai, K.; Tokura, Y. Néel-Type Skyrmion Lattice in the Tetragonal Polar Magnet $VOSe_2O_5$. *Phys. Rev. Lett.* **2017**, *119*, 237201. https://doi.org/10.1103/PhysRevLett.119.237201.
70. Singh, D.; Fujishiro, Y.; Hayami, S.; Moody, S.H.; Nomoto, T.; Baral, P.R.; Ukleev, V.; Cubitt, R.; Steinke, N.J.; Gawryluk, D.J.; et al. Transition between distinct hybrid skyrmion textures through their hexagonal-to-square crystal transformation in a polar magnet. *Nat. Commun.* **2023**, *14*, 8050. https://doi.org/https://doi.org/10.1038/s41467-023-43814-x.
71. Saha, S.R.; Sugawara, H.; Matsuda, T.D.; Sato, H.; Mallik, R.; Sampathkumaran, E.V. Magnetic anisotropy, first-order-like metamagnetic transitions, and large negative magnetoresistance in single-crystal Gd_2PdSi_3. *Phys. Rev. B* **1999**, *60*, 12162–12165. https://doi.org/10.1103/PhysRevB.60.12162.
72. Kurumaji, T.; Nakajima, T.; Hirschberger, M.; Kikkawa, A.; Yamasaki, Y.; Sagayama, H.; Nakao, H.; Taguchi, Y.; Arima, T.h.; Tokura, Y. Skyrmion lattice with a giant topological Hall effect in a frustrated triangular-lattice magnet. *Science* **2019**, *365*, 914–918. https://doi.org/10.1126/science.aau0968.
73. Hirschberger, M.; Spitz, L.; Nomoto, T.; Kurumaji, T.; Gao, S.; Masell, J.; Nakajima, T.; Kikkawa, A.; Yamasaki, Y.; Sagayama, H.; et al. Topological Nernst Effect of the Two-Dimensional Skyrmion Lattice. *Phys. Rev. Lett.* **2020**, *125*, 076602. https://doi.org/10.1103/PhysRevLett.125.076602.
74. Kumar, R.; Iyer, K.K.; Paulose, P.L.; Sampathkumaran, E.V. Magnetic and transport anomalies in R_2RhSi_3 (R = Gd, Tb, and Dy) resembling those of the exotic magnetic material Gd_2PdSi_3. *Phys. Rev. B* **2020**, *101*, 144440. https://doi.org/10.1103/PhysRevB.101.144440.

 doi:10.20944/preprints202511.0660.v1

75. Spachmann, S.; Elghandour, A.; Frontzek, M.; Löser, W.; Klingeler, R. Magnetoelastic coupling and phases in the skyrmion lattice magnet Gd_2PdSi_3 discovered by high-resolution dilatometry. *Phys. Rev. B* **2021**, *103*, 184424. https://doi.org/10.1103/PhysRevB.103.184424.
76. Gomilšek, M.; Hicken, T.J.; Wilson, M.N.; Franke, K.J.A.; Huddart, B.M.; Štefančič, A.; Holt, S.J.R.; Balakrishnan, G.; Mayoh, D.A.; Birch, M.T.; et al. Anisotropic Skyrmion and Multi-q Spin Dynamics in Centrosymmetric Gd_2PdSi_3. *Phys. Rev. Lett.* **2025**, *134*, 046702. https://doi.org/10.1103/PhysRevLett.134.046702.
77. Nakamura, S.; Kabeya, N.; Kobayashi, M.; Araki, K.; Katoh, K.; Ochiai, A. Spin trimer formation in the metallic compound $Gd_3Ru_4Al_{12}$ with a distorted kagome lattice structure. *Phys. Rev. B* **2018**, *98*, 054410. https://doi.org/10.1103/PhysRevB.98.054410.
78. Hirschberger, M.; Nakajima, T.; Gao, S.; Peng, L.; Kikkawa, A.; Kurumaji, T.; Kriener, M.; Yamasaki, Y.; Sagayama, H.; Nakao, H.; et al. Skyrmion phase and competing magnetic orders on a breathing kagome lattice. *Nat. Commun.* **2019**, *10*, 5831. https://doi.org/10.1038/s41467-019-13675-4.
79. Hirschberger, M.; Hayami, S.; Tokura, Y. Nanometric skyrmion lattice from anisotropic exchange interactions in a centrosymmetric host. *New J. Phys.* **2021**, *23*, 023039. https://doi.org/10.1088/1367-2630/abdef9.
80. Nakamura, S. Magnetic anisotropies and skyrmion lattice related to magnetic quadrupole interactions of the RKKY mechanism in the frustrated spin-trimer system $Gd_3Ru_4Al_{12}$ with a breathing kagome structure. *Phys. Rev. B* **2025**, *111*, 184433. https://doi.org/10.1103/PhysRevB.111.184433.
81. Santini, P.; Carretta, S.; Amoretti, G.; Caciuffo, R.; Magnani, N.; Lander, G.H. Multipolar interactions in f-electron systems: The paradigm of actinide dioxides. *Rev. Mod. Phys.* **2009**, *81*, 807–863. https://doi.org/10.1103/RevModPhys.81.807.
82. Kuramoto, Y.; Kusunose, H.; Kiss, A. Multipole orders and fluctuations in strongly correlated electron systems. *J. Phys. Soc. Jpn.* **2009**, *78*, 072001. https://doi.org/10.1143/JPSJ.78.072001.
83. Suzuki, M.T.; Ikeda, H.; Oppeneer, P.M. First-principles theory of magnetic multipoles in condensed matter systems. *J. Phys. Soc. Jpn.* **2018**, *87*, 041008. https://doi.org/10.7566/JPSJ.87.041008.
84. Kusunose, H.; Hayami, S. Generalization of microscopic multipoles and cross-correlated phenomena by their orderings. *J. Phys.: Condens. Matter* **2022**, *34*, 464002. https://doi.org/10.1088/1361-648x/ac9209.
85. Hayami, S.; Kusunose, H. Unified description of electronic orderings and cross correlations by complete multipole representation. *J. Phys. Soc. Jpn.* **2024**, *93*, 072001. https://doi.org/https://doi.org/10.7566/JPSJ.93.072001.
86. Suzuki, M.T.; Koretsune, T.; Ochi, M.; Arita, R. Cluster multipole theory for anomalous Hall effect in antiferromagnets. *Phys. Rev. B* **2017**, *95*, 094406. https://doi.org/10.1103/PhysRevB.95.094406.
87. Hayami, S.; Oiwa, R.; Kusunose, H. Electric Ferro-Axial Moment as Nanometric Rotator and Source of Longitudinal Spin Current. *J. Phys. Soc. Jpn.* **2022**, *91*, 113702. https://doi.org/10.7566/JPSJ.91.113702.
88. Hayami, S. Mechanism of antisymmetric spin polarization in centrosymmetric multiple-Q magnets based on effective chiral bilinear and biquadratic spin cross products. *Phys. Rev. B* **2022**, *105*, 024413. https://doi.org/10.1103/PhysRevB.105.024413.
89. Sukhachov, P.; Linder, J. Impurity-induced Friedel oscillations in altermagnets and p-wave magnets. *Phys. Rev. B* **2024**, *110*, 205114. https://doi.org/10.1103/PhysRevB.110.205114.
90. Brekke, B.; Sukhachov, P.; Giil, H.G.; Brataas, A.; Linder, J. Minimal Models and Transport Properties of Unconventional p-Wave Magnets. *Phys. Rev. Lett.* **2024**, *133*, 236703. https://doi.org/10.1103/PhysRevLett.133.236703.
91. Katsura, H.; Nagaosa, N.; Balatsky, A.V. Spin Current and Magnetoelectric Effect in Noncollinear Magnets. *Phys. Rev. Lett.* **2005**, *95*, 057205. https://doi.org/10.1103/PhysRevLett.95.057205.
92. Mostovoy, M. Ferroelectricity in Spiral Magnets. *Phys. Rev. Lett.* **2006**, *96*, 067601. https://doi.org/10.1103/PhysRevLett.96.067601.
93. Sergienko, I.A.; Dagotto, E. Role of the Dzyaloshinskii-Moriya interaction in multiferroic perovskites. *Phys. Rev. B* **2006**, *73*, 094434. https://doi.org/10.1103/PhysRevB.73.094434.
94. Harris, A.B.; Yildirim, T.; Aharony, A.; Entin-Wohlman, O. Towards a microscopic model of magnetoelectric interactions in $Ni_3V_2O_8$. *Phys. Rev. B* **2006**, *73*, 184433. https://doi.org/10.1103/PhysRevB.73.184433.
95. Tokura, Y.; Seki, S.; Nagaosa, N. Multiferroics of spin origin. *Rep. Prog. Phys.* **2014**, *77*, 076501. https://doi.org/10.1088/0034-4885/77/7/076501.
96. Hirsch, J.E. Spin Hall Effect. *Phys. Rev. Lett.* **1999**, *83*, 1834–1837. https://doi.org/10.1103/PhysRevLett.83.1834.
97. Zhang, S. Spin Hall Effect in the Presence of Spin Diffusion. *Phys. Rev. Lett.* **2000**, *85*, 393–396. https://doi.org/10.1103/PhysRevLett.85.393.

98. Murakami, S.; Nagaosa, N.; Zhang, S.C. Dissipationless quantum spin current at room temperature. *Science* **2003**, *301*, 1348–1351. https://doi.org/10.1126/science.1087128.
99. Murakami, S.; Nagaosa, N.; Zhang, S.C. Spin-Hall Insulator. *Phys. Rev. Lett.* **2004**, *93*, 156804. https://doi.org/10.1103/PhysRevLett.93.156804.
100. Sinova, J.; Culcer, D.; Niu, Q.; Sinitsyn, N.A.; Jungwirth, T.; MacDonald, A.H. Universal Intrinsic Spin Hall Effect. *Phys. Rev. Lett.* **2004**, *92*, 126603. https://doi.org/10.1103/PhysRevLett.92.126603.
101. Kusunose, H.; Oiwa, R.; Hayami, S. Complete Multipole Basis Set for Single-Centered Electron Systems. *J. Phys. Soc. Jpn.* **2020**, *89*, 104704. https://doi.org/10.7566/JPSJ.89.104704.
102. Takagi, R.; White, J.; Hayami, S.; Arita, R.; Honecker, D.; Rønnow, H.; Tokura, Y.; Seki, S. Multiple-q noncollinear magnetism in an itinerant hexagonal magnet. *Sci. Adv.* **2018**, *4*, eaau3402. https://doi.org/10.1126/sciadv.aau3402.
103. Kim, J.; Zhang, K.X.; Park, P.; Cho, W.; Kim, H.; Noh, H.J.; Park, J.G. Electrical control of topological 3Q state in intercalated van der Waals antiferromagnet Co_x-TaS_2. *Nat. Commun.* **2025**, *16*, 8943. https://doi.org/https://doi.org/10.1038/s41467-025-63991-1.
104. Meng, Z.; Lin, W.; Zhao, Z.; Zhang, B.; Li, B.; Lv, Y.; Han, G.; Li, S.; Cai, Y.; Jin, F.; et al. Spontaneous Topological Hall Effect in Intercalated $Co_{1/3}TaS_2$ Nanoflakes with Non-Coplanar Antiferromagnetic Order. *Adv. Func. Mater.* **2025**, p. 2502016. https://doi.org/https://doi.org/10.1002/adfm.202502016.
105. Park, P.; Cho, W.; Kim, C.; An, Y.; Iida, K.; Kajimoto, R.; Matin, S.; Zhang, S.S.; Batista, C.D.; Park, J.G. Spin Dynamics of Triple-**Q** Magnetic Orderings in a Triangular Lattice: Implications for Multi-**Q** Orderings in General Two-Dimensional Lattices. *Phys. Rev. X* **2025**, *15*, 031032. https://doi.org/10.1103/y9ly-4kld.
106. Bulaevskii, L.N.; Batista, C.D.; Mostovoy, M.V.; Khomskii, D.I. Electronic orbital currents and polarization in Mott insulators. *Phys. Rev. B* **2008**, *78*, 024402. https://doi.org/10.1103/PhysRevB.78.024402.
107. Vanderbilt, D. *Berry phases in electronic structure theory: electric polarization, orbital magnetization and topological insulators*; Cambridge University Press, Cambridge, 2018.
108. Resta, R.; Ceresoli, D.; Thonhauser, T.; Vanderbilt, D. Orbital magnetization in extended systems. *Chem. Phys. Chem.* **2005**, *6*, 1815–1819. https://doi.org/https://doi.org/10.1002/cphc.200400641.
109. Xiao, D.; Shi, J.; Niu, Q. Berry Phase Correction to Electron Density of States in Solids. *Phys. Rev. Lett.* **2005**, *95*, 137204. https://doi.org/10.1103/PhysRevLett.95.137204.
110. Thonhauser, T.; Ceresoli, D.; Vanderbilt, D.; Resta, R. Orbital Magnetization in Periodic Insulators. *Phys. Rev. Lett.* **2005**, *95*, 137205. https://doi.org/10.1103/PhysRevLett.95.137205.
111. Ceresoli, D.; Thonhauser, T.; Vanderbilt, D.; Resta, R. Orbital magnetization in crystalline solids: Multi-band insulators, Chern insulators, and metals. *Phys. Rev. B* **2006**, *74*, 024408. https://doi.org/10.1103/PhysRevB.74.024408.
112. Shi, J.; Vignale, G.; Xiao, D.; Niu, Q. Quantum Theory of Orbital Magnetization and Its Generalization to Interacting Systems. *Phys. Rev. Lett.* **2007**, *99*, 197202. https://doi.org/10.1103/PhysRevLett.99.197202.
113. Souza, I.; Vanderbilt, D. Dichroic f-sum rule and the orbital magnetization of crystals. *Phys. Rev. B* **2008**, *77*, 054438. https://doi.org/10.1103/PhysRevB.77.054438.
114. Yamasaki, Y.; Nakao, H.; Arima, T.h. Augmented Magnetic Octupole in Kagomé 120-degree Antiferromagnets Detectable via X-ray Magnetic Circular Dichroism. *J. Phys. Soc. Jpn.* **2020**, *89*, 083703. https://doi.org/10.7566/JPSJ.89.083703.
115. Hayami, S.; Kusunose, H. Essential role of the anisotropic magnetic dipole in the anomalous Hall effect. *Phys. Rev. B* **2021**, *103*, L180407. https://doi.org/10.1103/PhysRevB.103.L180407.
116. Kimata, M.; Sasabe, N.; Kurita, K.; Yamasaki, Y.; Tabata, C.; Yokoyama, Y.; Kotani, Y.; Ikhlas, M.; Tomita, T.; Amemiya, K.; et al. X-ray study of ferroic octupole order producing anomalous Hall effect. *Nat. Commun.* **2021**, *12*, 5582. https://doi.org/https://doi.org/10.1038/s41467-021-25834-7.
117. Sasabe, N.; Kimata, M.; Nakamura, T. Presence of X-Ray Magnetic Circular Dichroism Signal for Zero-Magnetization Antiferromagnetic State. *Phys. Rev. Lett.* **2021**, *126*, 157402. https://doi.org/10.1103/PhysRevLett.126.157402.
118. Ohgata, S.; Hayami, S. Intrinsic anomalous Hall effect under anisotropic magnetic dipole versus conventional magnetic dipole. *Phys. Rev. B* **2025**, *112*, 014421. https://doi.org/10.1103/8xv3-18nr.
119. Dubovik, V.; Cheshkov, A. Multipole expansion in classical and quantum field theory and radiation. *Sov. J. Part. Nucl* **1975**, *5*, 318–337.
120. Dubovik, V.; Tugushev, V. Toroid moments in electrodynamics and solid-state physics. *Phys. Rep.* **1990**, *187*, 145–202. https://doi.org/10.1016/0370-1573(90)90042-Z.

 doi:10.20944/preprints202511.0660.v1

121. Hlinka, J. Eight Types of Symmetrically Distinct Vectorlike Physical Quantities. *Phys. Rev. Lett.* **2014**, *113*, 165502. https://doi.org/10.1103/PhysRevLett.113.165502.
122. Hlinka, J.; Privratska, J.; Ondrejkovic, P.; Janovec, V. Symmetry Guide to Ferroaxial Transitions. *Phys. Rev. Lett.* **2016**, *116*, 177602. https://doi.org/10.1103/PhysRevLett.116.177602.
123. Cheong, S.W.; Lim, S.; Du, K.; Huang, F.T. Permutable SOS (symmetry operational similarity). *npj Quantum Mater.* **2021**, *6*, 58. https://doi.org/10.1038/s41535-021-00346-1.
124. Cheong, S.W.; Huang, F.T.; Kim, M. Linking emergent phenomena and broken symmetries through one-dimensional objects and their dot/cross products. *Rep. Prog. Phys.* **2022**, *85*, 124501. https://doi.org/10.1088/1361-6633/ac97aa.
125. Nasu, J.; Hayami, S. Antisymmetric thermopolarization by electric toroidicity. *Phys. Rev. B* **2022**, *105*, 245125. https://doi.org/10.1103/PhysRevB.105.245125.
126. Roy, A.; Guimarães, M.H.D.; Sławińska, J. Unconventional spin Hall effects in nonmagnetic solids. *Phys. Rev. Materials* **2022**, *6*, 045004. https://doi.org/10.1103/PhysRevMaterials.6.045004.
127. Inda, A.; Hayami, S. Nonlinear Transverse Magnetic Susceptibility under Electric Toroidal Dipole Ordering. *J. Phys. Soc. Jpn.* **2023**, *92*, 043701. https://doi.org/https://doi.org/10.7566/JPSJ.92.043701.
128. Jin, W.; Drueke, E.; Li, S.; Admasu, A.; Owen, R.; Day, M.; Sun, K.; Cheong, S.W.; Zhao, L. Observation of a ferro-rotational order coupled with second-order nonlinear optical fields. *Nat. Phys.* **2020**, *16*, 42–46. https://doi.org/10.1038/s41567-019-0695-1.
129. Hayashida, T.; Uemura, Y.; Kimura, K.; Matsuoka, S.; Hagihala, M.; Hirose, S.; Morioka, H.; Hasegawa, T.; Kimura, T. Phase transition and domain formation in ferroaxial crystals. *Phys. Rev. Materials* **2021**, *5*, 124409. https://doi.org/10.1103/PhysRevMaterials.5.124409.
130. Hayashida, T.; Uemura, Y.; Kimura, K.; Matsuoka, S.; Morikawa, D.; Hirose, S.; Tsuda, K.; Hasegawa, T.; Kimura, T. Visualization of ferroaxial domains in an order-disorder type ferroaxial crystal. *Nat. Commun.* **2020**, *11*, 4582. https://doi.org/10.1038/s41467-020-18408-6.
131. Yokota, H.; Hayashida, T.; Kitahara, D.; Kimura, T. Three-dimensional imaging of ferroaxial domains using circularly polarized second harmonic generation microscopy. *npj Quantum Mater.* **2022**, *7*, 106. https://doi.org/10.1038/s41535-022-00515-w.
132. Hasegawa, T.; Yoshida, W.; Nakamura, K.; Ogita, N.; Matsuhira, K. Raman Scattering Investigation of Structural Transition in $Ca_5Ir_3O_{12}$. *J. Phys. Soc. Jpn.* **2020**, *89*, 054602. https://doi.org/10.7566/JPSJ.89.054602.
133. Hanate, H.; Hasegawa, T.; Hayami, S.; Tsutsui, S.; Kawano, S.; Matsuhira, K. First Observation of Superlattice Reflections in the Hidden Order at 105 K of Spin–Orbit Coupled Iridium Oxide $Ca_5Ir_3O_{12}$. *J. Phys. Soc. Jpn.* **2021**, *90*, 063702. https://doi.org/10.7566/JPSJ.90.063702.
134. Hayami, S.; Tsutsui, S.; Hanate, H.; Nagasawa, N.; Yoda, Y.; Matsuhira, K. Cluster Toroidal Multipoles Formed by Electric-Quadrupole and Magnetic-Octupole Trimers: A Possible Scenario for Hidden Orders in $Ca_5Ir_3O_{12}$. *J. Phys. Soc. Jpn.* **2023**, *92*, 033702. https://doi.org/https://doi.org/10.7566/JPSJ.92.033702.
135. Hanate, H.; Tsutsui, S.; Yajima, T.; Nakao, H.; Sagayama, H.; Hasegawa, T.; Matsuhira, K. Space-Group Determination of Superlattice Structure Due to Electric Toroidal Ordering in $Ca_5Ir_3O_{12}$. *J. Phys. Soc. Jpn.* **2023**, *92*, 063601. https://doi.org/https://doi.org/10.7566/JPSJ.92.063601.
136. Xu, X.; Huang, F.T.; Admasu, A.S.; Kratochvílová, M.; Chu, M.W.; Park, J.G.; Cheong, S.W. Multiple ferroic orders and toroidal magnetoelectricity in the chiral magnet $BaCoSiO_4$. *Phys. Rev. B* **2022**, *105*, 184407. https://doi.org/10.1103/PhysRevB.105.184407.
137. Inda, A.; Hayami, S. Emergent cross-product-type spin-orbit coupling under ferroaxial ordering. *Phys. Rev. B* **2025**, *111*, L041104. https://doi.org/10.1103/PhysRevB.111.L041104.